# POLITECNICO DI TORINO
## Repository ISTITUZIONALE

Advanced Data Chain Technologies for the Next Generation of Earth Observation Satellites Supporting On-Board Processing for Rapid Civil Alerts

(Article begins on next page)

08 November 2022

IAC-21-B5.1.3

# Advanced Data Chain Technologies for the Next Generation of Earth Observation Satellites Supporting On-Board Processing for Rapid Civil Alerts

**M. Kerr[1*], J. I. Bravo[1], R. Hinz[1], F. Membibre[1], A. Ramos[1], A. Morón[1], A. Latorre[1], Helko Breit[2], Stefan Wiehle[2], Dominik Guenzel[2], Otto Koudelka[3], Franz Teschl[3], Enrico Magli[4], Michele Caon[4], Tiziano Bianchi[4], Maurizio Martina[4], R. Freddi[5], F. Milani[5], G. Curci[5], Cecilia Marcos[6]**

[1] *DEIMOS Space S.L.U., Tres Cantos – Madrid, Spain, Email: {murray.kerr, juan-ignacio.bravo, robert.hinz, francisco.membibre, alvaro.moron, antonio.latorre}@deimos-space.com*
[2] *Deutsches Zentrum für Luft- und Raumfahrt e.V., Germany, Email: {helko.breit, stefan.wiehle, Dominik.Guenzel}@dlr.de*
[3] *Technische Universität Graz, Graz, Austria, Email: koudelka@tugraz.at, franz.teschl@tugraz.at*
[4] *Politecnico di Torino, Turin, Italy, Email: {enrico.magli, michele.caon, tiziano.bianchi, aurizio.martina}@polito.it*
[5] *OHB Italia Spa, Milan, Italy, Email: {rfreddi, fmilani.ext, gcurci.ext}@cgspace.it*
[6] *Agencia Estatal de Meteorología, Spain – cmarcosm@aemet.es*
\* Corresponding Author

## Abstract

The growing number of planned Earth Observation (EO) satellites, together with the increase in payload resolution and swath, brings to the fore the generation of unprecedented volumes of data that needs to be downloaded, processed and distributed with low latency. This creates a severe bottleneck problem, which overloads ground infrastructure, communications to ground, and hampers the provision of EO products to the End User with the required performances.

The European H2020 EO-ALERT project (http://eo-alert-h2020.eu/), proposes the definition of **next-generation EO missions** by developing an **on-board high speed EO data processing chain**, based on a novel flight segment architecture that moves optimised key EO data processing elements from the ground segment to on-board the satellite. EO-ALERT achieves, globally, latencies **below five minutes** for EO products delivery, reaching latencies **below 1 minute** in some scenarios.

The proposed architecture solves the above challenges through a combination of innovations in the on-board elements of the data chain and the communications link. Namely, the architecture introduces innovative technological solutions, including on-board **reconfigurable data handling**, on-board **image generation** and **processing** for generation of alerts (EO products) using **Artificial Intelligence (AI)**, **high-speed on-board avionics**, on-board **data compression and encryption using AI** and **reconfigurable high data rate communication** links to ground including a separate chain for alerts with minimum latency and global coverage. Those key technologies have been studied, developed, implemented in software/hardware (SW/HW) and verified against previously established technologies requirements to meet the identified user needs.

The paper presents an overview of the development of the innovative solutions defined during the project for each of the above-mentioned technological areas and the results of the testing campaign of the individual SW/HW implementations within the context of two operational scenarios: **ship detection** and **extreme weather observation** (nowcasting), both requiring a high responsiveness to events to reduce the response time to few hours, or even to minutes, after an emergency situation arises.

The technologies have been experimentally evaluated during the project using relevant EO historical sensor data. The results demonstrate the maturity of the technologies, having now reached TRL 4-5. Generally, the results show that, when implemented using COTS components and available communication links, the proposed architecture can generate and deliver globally EO products/alerts with a **latency lower than five minutes**, which demonstrates the viability of the EO-ALERT concept. The paper also discusses the implementation on an Avionic Test Bench (ATB) for the validation of the integrated technologies chain.

**Keywords:** Satellite Architecture, Earth Observation, On-Board Processing, AI, Real-Time, Low Latency

**Acronyms/Abbreviations**

| | | | |
|---|---|---|---|
| AI | = Artificial Intelligence | VHR | = Very High Resolution |
| ATB | = Avionics Test-Bench | MPSoC | = Multiprocessor System on a Chip |
| CCSDS | = Consultative Committee for Space Data Systems | MSG | = Meteosat Second Generation |
| COTS | = Commercial Off-The-Shelf | OT | = Overshooting Top |
| CPU | = Central Processing Unit | PL | = Programmable Logic |
| CS-CEDH | = CPU Scheduling, Compression, Encryption and Data Handling | PS | = Processing System |
| | | SAR | = Synthetic Aperture Radar |
| EO | = Earth Observation | SEVIRI | = Spinning Enhanced Visible and Infrared Imager |
| GEO | = Geostationary | | |
| | | TRL | = Technology Readiness Level |

## 1. Introduction

Recent years have seen a sharp growth in Satellite Earth Observation (EO) product applications, such as environment and resource monitoring, emergency management and civilian security, leading to an increase in demands on amount, type and quality of remote-sensing satellite data.

Many of these EO applications require low latency product delivery to the end user, which is limited by the amount of EO raw data generated on-board the satellite and the severe bottleneck created by the classical EO data processing chain which involves the acquisition of sensor data on-board the satellite, its compression and storage on-board, and its transfer to ground for later processing on ground and the generation of the downstream EO image products.

The EO-ALERT project (http://eo-alert-h2020.eu/), an H2020 European Union research activity addresses the challenge of a high-speed data chain and the need for increased EO data chain throughput. EO-ALERT proposes the definition and development of the next-generation EO data and processing chain, based on a novel flight segment architecture that moves optimised key EO data processing elements from the ground segment to on-board the satellite. The objective is to deliver globally EO products to the end user with very low latencies for increased throughput [1].

In order to meet this goal, EO-ALERT introduces an innovative reconfigurable data handling architecture which integrates different onboard technologies for both Synthetic Aperture Radar (SAR) and optical sensor data, including image generation, image processing for rapid alerts, joint compression and encryption algorithms.

Two application scenarios are used to demonstrate the capabilities of the EO-ALERT architecture: Ship detection and monitoring which is motivated by the European Maritime Safety Agency's (EMSA) vessel detection service and offers possible applications for monitorization of illegal fishing, illegal immigration and in search and rescue missions; and meteorological nowcasting and very short-range forecasting for early warnings of convective storms, inspired by the NWCSAF Rapid Developing Thunderstorms – Convection Warning (RDT-CW) product [2].

This paper presents the results of the experimental evaluation of the innovative elements of EO-ALERT's data processing chain for these two use-case scenarios and discusses the implementation on an Avionic Test Bench (ATB) for the validation of the integrated technologies chain. The aim is to demonstrate that EO-ALERT reaches Technology Readiness Level (TRL) 4-5 maturity for the on-board architecture and technologies.

The remainder of the article is structured as follows: After an overview of the project objectives and application scenarios in Section 2, a summary of the EO-ALERT functional architecture, described in greater detail in [3], and a description of the Avionic Test Bench is given in Section 3. Section 4 reports the results of the implementation and system tests of the advanced data chain technologies carried out for onboard optical and SAR image generation and processing (Sections 4.1 and 4.2), onboard compression and data handling (Section 4.3), communications (Section 4.4) and the Avionic Test Bench (4.5). The conclusions are summarized in Section 0.

The focus of this paper is on the verification results of the test campaign and only briefly introduces the functional architecture and implementation details. A detailed description on these topics can be found in [3]. Information on the definition of the user requirements for the EO-ALERT EO data processing chain, a high-level mission analysis, the concept of operations, and the experimental campaign carried out to collect ground-truth data is given in [4].

## 2. Objectives, Application Scenarios and Datasets

The two reference scenarios which are used in EO-ALERT to test and demonstrate, using real satellite and EO payload data, the correctness of the architecture and the performance of the system, are presented in the following

### 2.1 Ship Detection Scenario

The main driver of the ship detection scenario is to develop on-board the satellite an alert, similar to the EMSA Vessel Detection System (VDS), and send this directly to an end user globally with a very short latency (goal of 1 minute, requirement below 5 minutes). The ship characteristics reported in the alert include:

❑ Position & movement (velocity, heading).

❑ Ship details (size, width, etc)

❑ Ship image (clipping thumbnail)

The dataset used for training and testing in the optical ship detection scenario consists of 40 VHR optical acquisitions obtained from the DEIMOS-2 satellite, in both raw and L1B formats. Each acquisition is manually annotated to obtain the vessel position in the image. The remaining vessel details included in the alert are validated using AIS data corresponding to the acquisition.

Ship detection from SAR uses SAR (TerraSAR-X) satellite data in single-polarization StripMap mode to derive the desired information directly from the sea surface. A total of nine scenes from five acquisitions taken in 2016 and 2017 in the Mediterranean Sea were selected for the development and verification of the SAR extreme weather scenario. Each scene has a size of at least 12.5 km along-track and 30 km in ground range with pixel size around 3-4 m, resulting in spatial coverage of 375 km² to 500 km².

Numerical weather prediction data from the Global Forecast System (GFS) is used to validate the wind speed estimations. In addition, the on-board results are compared with those obtained from ground-based TerraSAR-X MGD products using operational algorithms.

### 2.2 Extreme Weather Scenario

For the extreme weather scenario, two types of detections have been considered: convective storms and wind speed.

Convective Storm Nowcasting: A very low latency meteorological nowcasting service for severe convective storms was selected as one of the extreme weather scenarios. The goal is to implement the functionality of operational convective storm detection systems like NWCSAF's RDT-CW (Rapidly

Developing Thunderstorms – Convection Warning) [2] on-board and send an alert directly to the end user.

For the development and verification of the convective storm detection a dataset created from MSG High Rate SEVIRI Level 1.5 data is used. Optical image generation from raw data is performed and tested for the EO-ALERT ship scenario. The images correspond to 164 days in 62 periods of one or more consecutive days between 2016 and 2018. Images have size 1192pxl x 639pxl with a ground sampling distance of 3 km/px, covering a total area 6.855.192 km² containing the European continent. Of the 12 available SEVIRI channels, 5 are used for the generation of the data set.
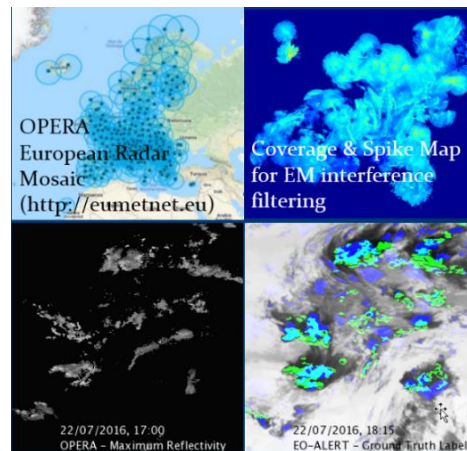


**Figure 1: Ground Truth data generation from OPERA radar data.**

Ground truth data for training and testing of the ML algorithm is generated from OPERA weather radar network maximum reflectivity data [5]. Spurious radar echoes caused by EM interferences are removed from radar images using a clutter map. Mature convective cells in each radar image are detected applying the algorithm described in [6]. After re-projecting OPERA images to the MSG grid, a tracked candidate cell is labelled convective if it overlaps with OPERA convective cells at any time. See [7] for more details.

For cells classified as convective all candidate cells identified, the system also detects overshooting tops (OTs). This phenomenon consists of deep convective storm updrafts forming dome-like structures above the convective cells which are directly related to hazardous weather at the Earth's surface such as heavy rainfall, damaging winds, large hail, and tornadoes [8], making an early detection of these kinds of phenomena beneficial in many senses. The ground truth used for OT classification is an expert-annotated dataset created by Setvák et al. [9] based on MSG SEVIRI images of 2.5-minute rapid scan tests acquired on 20th June 2013 and 29th July 2013 and complemented by lightning detection data. The first date contains 1365, the second 446 OTs.

Wind Speed and Sea State: A very low latency maritime wind speed and wave height service was selected as another extreme weather scenario. This uses the same SAR (TerraSAR-X) satellite data as the SAR ship detection scenario described in Section 2.1.

## 3. Functional Architecture

Figure 1 shows the high-level functional architecture implemented in EO-ALERT. To achieve the target latency in EO products delivery, the proposed functional architecture includes several innovative elements: on-board processing of the payload raw data to L1, processing of the on-board L1 product to generate the EO product (e.g. ship detection alert), reconfigurable data handling to prioritise the EO products over raw data, and multiple communications channels, to provide for a global alerts (EO product) delivery via a satellite-relay and a traditional bulk raw data delivery service via direct to ground links (Ka-band).
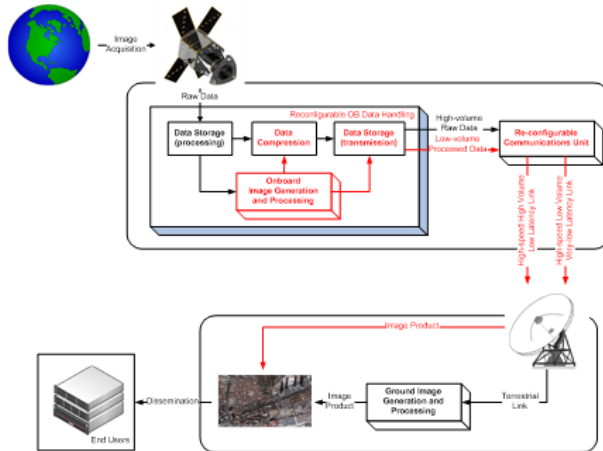


**Figure 2: EO-ALERT's next generation satellite processing chain for rapid civil alerts introduces new innovative key elements and data flows (red).**

To ensure the system is suitable for several mission scenarios and multiple payload types, the functional architecture is designed to be modular, scalable and reconfigurable. The entire data-chain is divided into several functional blocks, each one implemented on dedicated software and/or hardware computing resources. Each function can be configured or changed with no or little impact on the others, and the available processing power can be assigned to each function based on the mission requirements. With this approach, the system can process different data types (e.g., optical and SAR data) from several sensors, over a wide range of dataset sizes.

More information on the functional elements implemented and verified in the EO-ALERT project can be found in [1], [10], [11] and [12].

### 3.1 Optical Image Generation and Processing

The **O/B Optical Image Generation** provides a HR image product for latency-driven scenarios and enables the **Image Processing** stage by generating a denoised and artifact-free image. The O/B L1 product consists of: 1) HR calibrated and denoised image, 2) geolocation information, 3) HR sea-land binary mask (3m/pixel). The raw data obtained from the payload is calibrated to remove pixel inconsistencies and to convert the pixel digital counts to radiances. The calibrated image is processed with an edge-aware denoising algorithm based on optimised convolutional operations. The position provided by the satellite GPS and the attitude provided by the AOCS are used to geolocate the image corners. The geolocation algorithm is prepared to integrate Earth Orientation Parameters that can be sent to the spacecraft. The geolocation information is used to retrieve the sea-land pixel binary mask that is stored on-board. To avoid decompressing the whole land-mask on-board, which could lead to memory issues, the minimum chunk of information required to generate the sea-land mask for the image is extracted and decompressed on the O/B memory. The sea-land mask is projected onto the image coordinates to assign sea-land information to the image pixels.

The **ship detection algorithm** is applied to HR panchromatic images and consists of a 3-step approach: 1) candidate ship extraction, 2) AI-based ship discrimination, 3) fusion. The first step provides regions of the image that have ship-alike shapes and intensities, using Otsu thresholding [13] combined with intensity and shape metrics. This information is fused with the land-sea mask to remove areas detected over land regions. In the ship discrimination step, each image region from the binary image is labelled independently using the algorithm from [14]. The regions from the image, corresponding to the labels from the binary image, are classified to assess the presence of a ship. The last step, fusion, removes ships detected on overlapping areas of the image (if the image is divided over different boards) or to suppress different detections of the same object.

In the **extreme weather scenario**, convective storms are detected from GEO satellite images using a 3-step algorithm: 1) candidate cell extraction, 2) candidate cell tracking, 3) AI-based convective cell discrimination. Candidate convective cells are detected as local temperature minima in brightness temperature images derived from GEO satellite data. Cell position and velocity are tracked over time by matching candidate cells between images of subsequent acquisitions based on spatial overlap in the corresponding maps. Ambiguities in the assignment due to cell merging or splitting are filtered to produce unique tracks. Machine

learning classifiers, trained on the ground truth data described in Section 2.2, perform convective cell discrimination. Each cell is characterized by its brightness temperatures in 5 infrared channels in SEVIRI imagery and their evolution over time. For cells classified as convective, the system also detects OTs using machine learning-based classification on image features extracted from subregions of the convective cell [15].

### 3.2 SAR Image Generation and Processing

Precise HR SAR image generation from satellite raw data is a complex and computationally expensive task. Considering TerraSAR-X as space segment, a full adaptation of the existing focusing processor, which uses the Chirp Scaling algorithm [16], is not foreseen. Based on the EO-ALERT objectives, the wave number domain Omega-K (ωKA) algorithm [17] ("monochromatic ωKA" approximate version) is selected to enable SAR image formation with resolution below 3m. **SAR image generation** covers signal processing of the sensor data and computation of processing and annotation parameters. Signal processing, such as raw data correction, Fast Fourier Transform/Inverse Fast Fourier Transform, antenna pattern correction, detection and multi-looking, demands high computation power, resources and input/output throughput; for this reason, this part of the algorithm is implemented in the MPSoC PL with parallelization. Processing and annotation parameters, such as geometric doppler centroid determination, SAR focusing parameter and geolocation, are calculated on the MPSoC PS ARM cores in software.

The **ship detection algorithm** [18] involves three image processing steps: 1) initial detection, 2) refinement, 3) filtering. A Constant False Alarm Rate algorithm is used in the first step. Each pixel intensity has to be compared to the mean intensity of its surrounding area: this step is computationally very expensive and it is implemented in hardware. The refinement step investigates the surrounding of all ship candidates to find additional ships close-by which were missed in the initial detection. Filtering removes azimuth ambiguities created during the image processing and applies land masking to remove all detections on land. Detections left after this step are considered detected ships and their properties (e.g., location, dimensions, heading) are gathered.

For the **extreme weather scenario**, the ocean surface wind speed and wave height are derived from the SAR image processing in three steps: 1) image tiling, 2) wind speed detection, 3) sea state detection. The image is divided into a grid of sub-scenes of configurable size, and wind and sea state detection are performed on each individual sub-scene. Wind speed

detection employs the Geophysical Model Function XMOD2 [19] previously tuned on TerraSAR-X archived images, calculating wind speed form sea surface backscatter. For sea state detection, the empirical XWAVE algorithm [20] is used. The resulting product includes wind speed and wave height on a per-sub-scene basis.

### 3.3 Compression, Encryption and Data Handling

One of the on-board MPSoC, the CS-CEDH Board, is dedicated to scheduling, data handling and compression and encryption tasks. The multithreaded application software running on the general-purpose CPU available on the PS of the device is responsible for the following operations:

- Acquire the optical or SAR raw data from the Sensor Board and ancillary data from the on-board ancillary data source, and forward the raw, ancillary and configuration data to the target optical or SAR Image Processing modules.

- Acquire EO products (e.g., alerts, generated images, etc.) from the Image Processing modules once they are ready

- Compress and encrypt the acquired non-image data (e.g., alerts, ancillary data, etc.) using general-purpose software routines and forward image data to the hardware image compression accelerator instantiated in the PL part of the MPSoC.

- Store the compressed-encrypted data on the on-board mass storage device and remove data that is no longer needed.

- Select the data to be transmitted to the ground segment according to the mission requirements and forward it to the TX/RX Subsystem.

- Schedule all the above tasks so that high priority data (i.e., alerts) is processed and delivered to the end user as soon as possible.

On the other hand, **compression and encryption of optical and SAR raw sensor data and generated images** is achieved using a hardware implementation of a combined compression and encryption algorithm based on the CCSDS 123.0-B-2 standard [21]. The standard compression algorithm has been extended to embed image encryption by sign-randomization of the prediction residuals [22]. A flexible and reconfigurable digital IP core has been synthesized for the FPGA available on the PL part of the MPSoC using HLS, starting from a hardware-oriented software implementation. The resulting accelerator maintains most of the feature and runtime reconfigurability of a

software routine such as support for arbitrary image dimensions (including single- and multi-band) and selectable compression level (lossless and near-lossless), while achieving 5 to 7 times faster throughput compared to a software solution, as shown in [23]. The software running on the PS splits each image into tiles (sub-sets of along-track lines), each of which is compressed and encrypted individually by the hardware IP core. This allows most of the image to be successfully reconstructed on the ground segment when some data is lost while transmitting the image to the ground segment, since only the tiles affected by the transmission errors will be corrupted. This solution was shown to have a negligible impact on the compression efficiency (typically <1% with 128-line tiles). Tiling also enables parallel image compression and encryption on target platforms with enough hardware resources to fit multiple IP cores in their PL. Image tiles and other non-alert data (e.g., ancillary data) are scheduled for transmission to the TX/RX Subsystem in a low priority queue, that is stalled when some high priority data (i.e., alerts) is ready for transmission. Each compressed-encrypted element is split into a stream of CCSDS packets that is atomically delivered to the TX/RX Subsystem over a high-speed communication channel (1Gbit/s Gigabit Ethernet link on the target platform). On-the-flight packetization was shown to have negligible impact on the transmission throughput, while image tiling allows high-priority data to be transmitted within 100ms from their availability in the transmission queue in all scenarios with 128-line image tiles.

Additional details about the compression, encryption, and data handling functionality of this board can be found in [23], [24], and [25].

### 3.4 Communications

The communications system delivers EO products, bulk (raw and generated image) data and alerts (O/B processed and generated) locally and globally at high speed with minimum latency. The latency requirement is 5 min for alerts for both local and global delivery, and 30 min for raw data/images for global delivery.
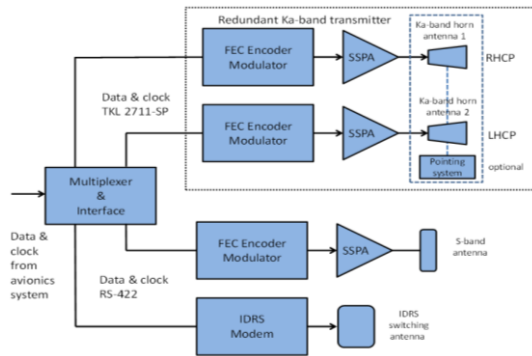


**Figure 3: Communications System Block Diagram**

The first high-speed data payload operates in Ka-band (25.5–27 GHz), which is assigned for EO and provides more bandwidth than X-band. The transmitter consists of a modem/codec (supporting QPSK, 8PSK, 16APSK and 64APSK modulation schemes) and an upconverter unit. 10W Ka-band solid-state power amplifier amplifies the signal and delivers it to a 25dBi-gain horn antenna. The system is fully redundant and supports data rates up to 2.6 Gbit/s (Figure 3).

The Ka-band system is used for both bulk data and alerts to local ground stations. The second payload consists of an S-band transmitter for alerts only, supporting data rates up to 1 Mbit/s to small and inexpensive hand-held terminals for rescue teams.

Bulk data can be delivered globally within 30 min via Ka-band, if a network of at least 13 ground stations around the globe is used. An alternative global broadband solution is the use of an optical terminal on board of the EO spacecraft and a data relay service such as the European Data Relay Satellite System (EDRS). Another solution for global delivery of alerts consists in using the INMARSAT satellite network and a compact product for the O/B transceiver provided by the company ADDVALUE [26] (iDRS service). The iDRS service is envisaged for the short-term EO-ALERT solution providing a data rate of 250 kbit/s. About 100 alerts can be transferred in 37 seconds.
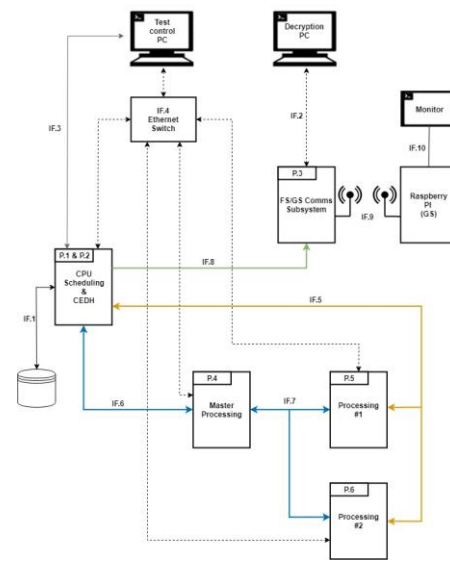
### 3.5 Avionics and Test Bench



**Figure 4: Test-Bench Architecture**

In order to perform the verification and validation activities of the EO-ALERT architecture, avionics test-bench (ATB) is employed (Figure 4). The ATB consists of a scaled-down version of the Avionics Subsystem, offering four boards instead of seven. To resemble the payload data processing unit (PDPU) as much as

possible, one board is dedicated CS-CEDH while the other three are dedicated to processing. TB boards are also interconnected, so that the complete data chain is reproduced and a realistic latency measurement can be obtained. A standard Gigabit Ethernet connection connects the TB to a TX/RX subsystem emulator to test the transmission to Ground Segment. The TB can be configured to process OPT or SAR data using an external PC and dedicated Ethernet links to each board. To inject real OPT and SAR data in the TB, raw images are loaded into an SSD connected to the CS-CEDH board, providing inputs that should come from sensors in the final system.

## 4. Results

### 4.1 Optical Image Generation and Processing

**Image Generation.** Each stage of the image generation process has been measured using a different metric, for which a total of 12 images in different conditions and cloud covers have been used for validation.

The process of radiometric calibration is compared against the operational Deimos-2 Product Processor output by means of the Structural Similarity Index Metric (SSIM). An average SSIM value of 0.98 is obtained.

The performance of the image denoising algorithm is measured in terms of Peak-Signal to Noise Ratio (PSNR) and SSIM under Gaussian noise with increasing standard deviation. Results are shown in Table 1.

**Table 1: PSNR and SSIM before and after denoising under increasing variance**

| Sigma (normalized) | Before denoising | | After denoising | |
|---|---|---|---|---|
| | PSNR (dB) | SSIM | PSNR (dB) | SSIM |
| 0.05 | 26.0202 | 0.3165 | 39.8944 | 0.9499 |
| 0.10 | 19.9997 | 0.1059 | 36.0452 | 0.9024 |
| 0.15 | 16.4783 | 0.0499 | 33.1188 | 0.8376 |
| 0.20 | 13.9780 | 0.0282 | 30.8510 | 0.7641 |
| 0.25 | 12.0405 | 0.0178 | 29.0335 | 0.6894 |
| 0.30 | 10.4581 | 0.0121 | 27.5064 | 0.6171 |
| 0.35 | 9.1187 | 0.0086 | 26.2017 | 0.5493 |
| 0.40 | 7.9585 | 0.0063 | 25.0120 | 0.4825 |
| 0.45 | 6.9359 | 0.0048 | 23.8058 | 0.4117 |
| 0.50 | 6.0206 | 0.0037 | 22.4821 | 0.3358 |

Finally, the geolocation process is measured against the output of the Deimos-2 Product Processor. The EO-ALERT on-board generation achieves an average error of ~45 meters compared to the Deimos-2 Product Processor using the same data inputs.

**Ship detection** performance and latency evaluation were performed over a test set consisting of 15 acquisitions. Each image consists of two sub-images from sensors with a resolution of 6000x13100px resulting in ~100km$^2$ observable areas with a resolution ~1m per px. Ground truth was created with manual annotations for ship detection and with the available AIS data for ship's details estimation.

**Detection performance** in terms of Probability of Detection (POD), False Alarm Ratio (FAR) and F1-score are shown in Table 2. The detection confidence level to consider a detection a ship was of 63%.

**Table 2:** Ship detection algorithm performance

| POD | FAR | F1 |
|---|---|---|
| 0.77 | 0.23 | 0.77 |

An example of ship detection is shown in Figure 5, where ship positions are given in latitude and longitude, and ship details such as length and width of the vessel are given in meters.



**Figure 5: Ship detection algorithm results.**

For performance and latency evaluation the **extreme weather** algorithm was executed on a test set consisting of MSG-SEVIRI images, setting a 366pxl x 366pxl region of interest (ROI) covering approximately 1,2x10$^6$ km$^2$ centered on the Iberian Peninsula. Ground truth data was derived from OPERA weather radar network maximum reflectivity data [5].

**Detection performance.** Results in terms of Probability of Detection (POD), False Alarm Ratio (FAR) and F1-score are shown in Table 3. The performance depends on the amount of available historical data, obtained by tracking each cell over up to 5 successive acquisitions in 15 min intervals. Results of the operational RDT product are shown for comparison. Due to the differences in the ground truth data and the classification strategy [2], [27], [28] the comparison should be considered as qualitative. The results suggest that for convective discrimination, the EO-ALERT EW

prototype product is compatible and can compete with the RDT-CW operational product.

**Table 3:** Extreme weather convective discrimination results on SEVIRI-OPERA test set.

| History (min) | POD | FAR | F1 |
|---|---|---|---|
| 0, -15, -30, -45, -60 | 0.82 | 0.14 | 0.84 |
| 0, -15, -30, -45 | 0.70 | 0.21 | 0.74 |
| 0, -15, -30 | 0.66 | 0.23 | 0.71 |
| 0, -15 | 0.59 | 0.25 | 0.66 |
| 0 | 0.47 | 0.29 | 0.57 |
| Combined | 0.68 | 0.20 | 0.73 |
| RDT v2011 | 0.74 | 0.34 | - |

OT detection is illustrated in Figure 6. In the left picture the ground truth of [9] can be seen, and in the right one, the prediction from the EO-ALERT OT detection algorithm. True positives are represented in green, false positives in red and false negatives in orange.
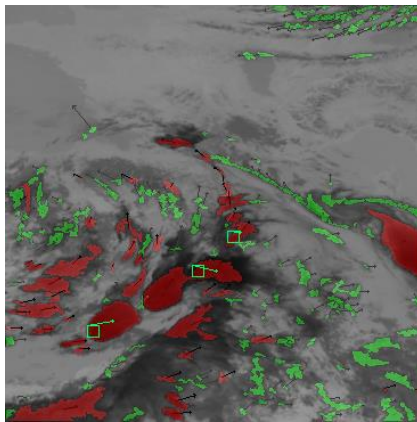


**Figure 6: OT detection algorithm results.**

**Table 4:** Extreme weather Overshooting Top detection

| POD | FAR | F1 |
|---|---|---|
| 0.501 | 0.448 | 0.525 |

Detection performance results from areas containing an OT which have been obtained over all detected candidate cells are shown in Table 4. The complete discrimination result, including convection and OT detection, is illustrated in Figure 7.



**Figure 7: Illustration of final detection result. Green: Non-convective cells. Red: Convective cells. Green boxes: Overshooting Top; green lines link the OT to the center of the cell. Arrows: Direction of cell movement.**

**Latencies.** Processing is performed in a dual-board scheme on only one processing board. Table 5 shows the time elapsed for candidate cell extraction, tracking and discrimination. Assuming additional transfer delays and management tasks, it is possible to have the products ready to be sent to ground in 6 seconds.

**Table 5:** Elapsed processing time for optical IP on the target hardware

| | Time (s) |
|---|---|
| Preprocessing | 1.9s |
| Candidate Extraction | 1.1s |
| Tracking | 0.4s |
| Discrimination | 0.9s |
| **Total Elapsed Time** | **4.3s** |

*4.2 SAR Image Generation and Processing*

**Image generation** was evaluated using TerraSAR-X data as the project does not include development of a new SAR instrument. However, because actual TerraSAR-X raw data was not to be used in the project, complex integer data for on-board processing was derived from complex TerraSAR-X SSC imagery via inverse SAR processing outside of the on-board system. While time-consuming, this task was necessary for implementation of the full SAR processing chain, which starts with raw data from the SAR instrument. For this reason, a raw data set of nine test scenes was first generated for on-board processing. The MSD images produced by on-board image generation were compared against their on-ground SSC counterparts.

**Image generation performance** of the SAR processing chain was evaluated with respect to radiometric and geometric accuracy. Across all test scenes, sigma0 of the on-board images was within 0.8 dB of the original TerraSAR-X SSC products in near, mid and far range. Geometric accuracy was investigated using point target analysis. In the worst case, geometric error of 6.5 m was measured, which is well within the project requirement of 10 m. Deviations occur due to usage of a low-resolution geoid model with small file size on-board compared to a high-resolution digital elevation model (DEM) on-ground.

**Latencies.** SAR image generation was performed in a single-board configuration. Table 6 lists the processing times of the steps for image generation for one scene of the test set. In this example, image generation took 3.7 s in total. The initial processing and annotation parameter calculation as well as geolocation were computed in 0.05 s in software on the PS. The Omega-K focusing algorithm, which was implemented in hardware on the PL, took 3.65 s. Image generation latency varied between 3.6 s and 4.1 s depending on the scene.
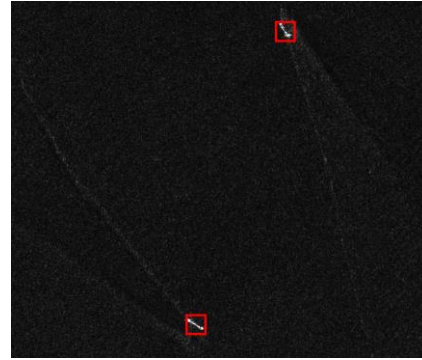
**Table 6: Processing times of SAR image generation for a block of 8192 x 24576 raw data pixels, which produces a 3488 x 8320 pixels large image with 419 km² coverage.**

|                         | Time (s) |
| ----------------------- | -------- |
| Parameters & Geolocation | 0.05     |
| Omega-K Focusing         | 3.65     |
| **Total Elapsed Time**   | 3.70     |

**Ship detection** performance and latency evaluation was performed using a set of nine test scenes generated on-board, each image having a size between 3424 to 3552 pixels in range and 6272 to 10112 pixels in azimuth. With pixel spacing in the range of 3-5 m, this results in coverage of 412-455 km² per scene. AIS data served as ground truth for validation of the generated ship alerts.

**Detection performance** of the SAR ship scenario was evaluated with regard to Probability of Detection (POD) and False Alarm Ratio (FAR). Across all test scenes, a total of 21 ships were present according to available AIS reference data. While there were also ships visible for which there was no AIS available, only those with complete reference data were considered for the calculation of POD. In the tested scenes, all 18 ships longer than 40 m were detected successfully, but shorter ships could not be detected reliably. With that, POD was 85.7 %. However, a low number of scenes and ergo ships was tested. FAR with regard to ship detection is defined as the number of falsely detected ships (false positive) relative to the total amount of detections. No false positives occurred in two of the test scenes. However, FAR exceeding 30 % or even 50 % has been measured for some of the other scenes. A closer look on these scenes revealed strong presence of azimuth land ghosts which have not been caught by the filtering mechanism. This source of errors is well-known from the original processing algorithm and not a result of the transfer to on-board processing. The occurrence of these azimuth ghosts is highest close to land and when, like done in preparation for the test scenes, land sections are removed from the full TerraSAR-X acquisition to focus on ocean areas. In operational use on the oceans with most acquisitions far away from land, FAR is expected to be below 5 %.

Figure 8 shows an example of SAR ship detection, where two ships have been detected in the visible area. For each ship an alert is triggered, containing the timestamp, position, length and width of the detected vessel as well as the confidence of detection.



**Figure 8: SAR ship detection algorithm results.**

**Latencies.** SAR image generation and ship detection were performed on a single board. Table 7 lists the processing times of the different steps for ship detection on one scene of the test set. In this example, image generation took 3.7 s, so that the latency of the full SAR sub-system was roughly 24 s. The total latency varies from 8 s to 28 s depending on the processed image because for scenes with a lot of land the initial detection step yields lots of potential ship candidates, which have to be filtered by the subsequent refinement and filtering stages.

**Table 7: Processing times of SAR ship detection for a 3488 x 8320 pixels large image with 419 km² coverage.**

|                        | Time (s) |
| ---------------------- | -------- |
| Preprocessing          | 3.7      |
| Initial Detection      | 3.8      |
| Refinement             | 8.8      |
| Filtering              | 4.3      |
| **Total Elapsed Time** | 20.6     |

**Extreme weather** performance and latency evaluation was performed using the same set of test scenes as for ship detection. Ground truth in this case was numerical weather prediction data from GFS for wind speed, but results were also compared with operational algorithms using ground-based SAR products.

**Detection performance** of the SAR weather scenario was evaluated with respect to deviation from ground reference. For all but one test scenes, the measured wind speed, averaged over the whole scene, was within 3 m/s of the ground truth model data. For one test scene, deviation was 5.6 m/s. In all cases, wind speed was over-estimated by the on-board system, so that the algorithm, which was originally intended for on-ground TerraSAR-X MGD scenes, may be adapted in future to the comparatively higher level of noise exhibited by the on-board images. Proper training would require a larger number of scenes than were available in this project, though. Regarding the on-ground reference, on-board wind speeds were also over-estimated, but

showed slightly better agreement. Comparatively higher deviations from the numerical model may be explained by its coarse temporal and spatial resolution, which hides occurrence of wind gusts and other natural phenomena.

**Latencies.** SAR image generation and weather detection were performed on a single board. Table 8 lists the processing times of the different steps for weather detection on one scene of the test set. In this example, image generation took 3.7 s, so that the latency of the full SAR sub-system was roughly 20 s. The total latency varies from 16 s to 38 s depending on the processed image because after the image tiling step measuring grid tiles which consist of more than 10 % land are not considered in the subsequent wind speed and sea state detection stages.

Table 8: Processing times of SAR weather detection for a 3488 x 8320 pixels large image with 419 km² coverage.

|  | Time (s) |
| --- | --- |
| Preprocessing | 1.1 |
| Image Tiling | 2.5 |
| Wind Speed Detection | 0.4 |
| Sea State Detection | 12.4 |
| **Total Elapsed Time** | 16.4 |

*4.3 Compression Encryption and Data Handling*

After being extensively tested through simulation with archive data, the CS-CEDH system described in Section 3.3 was deployed on one of the boards in the ATB, equipped with a Xilinx Zynq UltraScale+ ZU19EG MPSoC and tested with the dataset described in Section 2 in the intended scenarios (ship detection and extreme weather detection). A 200MHz clock frequency was chosen for the hardware image compression accelerator, as this led to the best throughput on the target platform [24]. The average compression-encryption latency per pixel obtained by the accelerator with 128-tiles from each supported data type during lossless compression (worst case for compression throughput) is reported in Table 9. The reported data takes into account the latency due to data movement between the CPU and the IP core, and so the overhead of tiling.

Table 9: Hardware image compression-encryption throughput @200MHz with 128-line tiles and lossless compression

| Data type | Raw data [ns/pixel] | Gen. image [ns/pixel] |
| --- | --- | --- |
| Optical, single band | $128.2 \pm 0.6$ | $100.6 \pm 0.3$ |
| Optical, 5-band | $138.0 \pm 1.7$ | $138.1 \pm 1.7$ |
| SAR | $260.4 \pm 1.1$ | $127.7 \pm 0.5$ |

As shown, the image compression accelerator achieves very low compression and encryption latencies

with all the image types supported by the EO-ALERT system, resulting in a throughput that is higher than 14.5MB/s with 16-bit samples in all cases except for SAR raw data. In this case, the effective throughput is halved because the real and imaginary parts of the image must be compressed and encrypted separately. The compression throughput is significantly higher when performing near-lossless compression, reaching 20MB/s (100ns/pixel) with the maximum absolute quantization error, 32.

The overhead of image tiling can be evaluated by comparing the results presented here with the raw hardware compression and encryption performance reported in [24], and ranges from 1% to 12% depending on the tile size: when processing smaller tiles (i.e., extracted from images with fewer pixels per line, such as optical multi-band data), the overhead of data transfers between the CPU and the IP core has a higher impact. This can be mitigated by selecting a higher number of lines per tile (larger tiles), at the cost of reduced tolerance to transmission errors.

The throughput of software general-purpose compression and encryption routines strongly depends on the number and priority of the operations scheduled on the CS-CEDH CPU, and during the tests was observed to range from 4MiB/s to 15MiB/s. To reduce the latency of alert delivery to the end user, alert encryption is always scheduled with the highest priority on each available CPU core, resulting in a more consistent throughput of 9MB/s to 14MB/s in most cases. Finally, the transmission throughput towards the TX/RX Subsystem is consistently higher than 800Mbit/s, confirming a negligible impact of on-the-flight packetization for what concerns the overall data chain latency. Refer to [25] for more detailed figures of merit about the software performance of the CS-CEDH module.

Thanks to the performance listed in the previous paragraphs, the CS-CEDH module can compress, encrypt, and deliver acquired and generated data with very low latency. Table 10 reports, for the most relevant data types, the overall latency from the moment a certain data is available on the CS-CEDH board to the moment its transmission to the TX/RX Subsystem is completed. Therefore, this latency considers all the operations performed on the board: internal and external data transfers, software and hardware compression and encryption, on-the-flight packetization, I/O operations. The reported latency was measured during the execution of each supported scenario on the EO-ALERT ATB. All images were compressed using lossless compression, and all the data was forwarded to the TX/RX Subsystem for transmission to the ground segment, so to represent a worst-case for latency. Because the multithreaded

software can process several data elements at the same time, sharing the computational resources among them, the reported latencies can be overlapped. As an example, the hardware accelerator can compress and encrypt the SAR raw data in about 50s, as reported in [25]. However, during the SAR test execution where the data in Table 10 was measured, the compression and encryption of the SAR raw data was interleaved with the compression and encryption of the SAR generated image. In other words, the time required to compress, encrypt, and transmit both the SAR raw data and the SAR generated image is lower than the sum of the corresponding latencies reported in Table 10.

**Table 10: Latency from data availability on the CS-CEDH board to the end of transmission to the TX/RX Subsystem**

| Data type | Optical, ship detection [s] | Optical, extreme weather [s] | SAR [s] |
|---|---|---|---|
| Raw data | 12.9 | 1.70 | 71.7 |
| Gen. image | 10.8 | 2.87 | 21.5 |
| Single alert | 0.0026 | 0.0052 | 0.0047 |

As shown, the contribution of the CS-CEDH board to overall data chain latency (from acquisition to product delivery to the end-user) is far lower than the 5min requirement, and therefore compatible with image processing and transmission latencies discussed in Sections 4.1, 4.2, and 4.4. In particular, the contribution of the CS-CEDH board to the alert data chain is negligible in all cases when compared to the alert generation latency on the image processing subsystems.

### 4.4 Communications

The transceiver/receiver communications subsystem emulator and communications hardware which is needed to test the transmission to the Ground Segment (GS) is shown in Figure 9. It uses both the satellite relay (L-band GEO-relay, Figure 11) and the different direct-to-ground channels (Ka-band and S-band, Figure 9 and Figure 10).



Figure 9: Communications Emulator for the complete subsystem: S-band transmitter, link controller for the iDRS transceiver, Ethernet switch and power supplies, with Ka-band emulated



Figure 10: Handheld device and touch screen for the direct Space-to-ground decryption and visualization (used for the S-band data link transfers)



Figure 11: iDRS unit terminal and receiver for the global persistent communications unit hardware in the test-bench

For the test of the iDRS link, the latencies range between 30 and 60 seconds, depending on the number of transmitted alerts, confirming that this solution is suitable for the EO-ALERT low-latency concept.

### 4.5 Testbench

A key outcome of the EO-ALERT project to date is that the performance of the data chain has been confirmed, both analytically and through hardware testing, covering the full data chain (payload to ground). This section presents the results of the project in terms of the current latency of the EO products, in the different reference scenarios.

#### Ship Detection Scenario Results

The ATB, including the communications units and emulator, have been used in ground testing to quantify the latency of the ship detection service.

For the ship scenario, the optical processing uses the optical DEIMOS-2 VHR satellite raw data. The testing is performed in a configurable multi-board scheme. Each board processes about 100 km$^2$ at ~0.9m resolution. To process this area, the entire on-board processing chain (Figure 12), from raw data to EO product delivery to the communications subsystem, takes less than 45 s running on a single Xilinx Zynq US+ board. Including the communication of alerts (ship detection and thumbnail image) through a global communications link, the total time is for alert generation and delivery is typically less than 1.5 minutes, and below 1 minute in the case that the number of alerts to be transmitted is small (i.e., less than 20 ship detection alerts). If the processing is parallelized over multiple boards, the ship service can be performed in less than 1 minute in all scenarios. More information on the optical processing chain for ship detection, and HW testing, can be found in [30], [31].
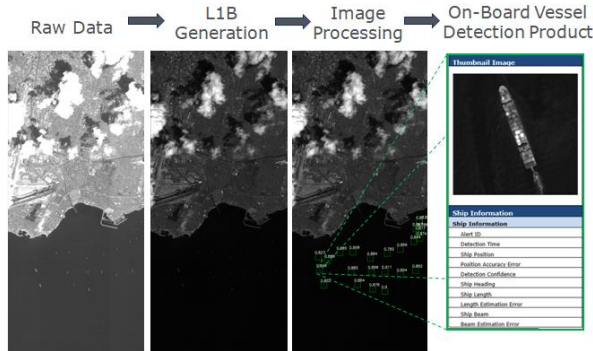


Figure 12: Optical on-board ship detection processing chain to the provision of EMSA VDS-like EO products (alerts).
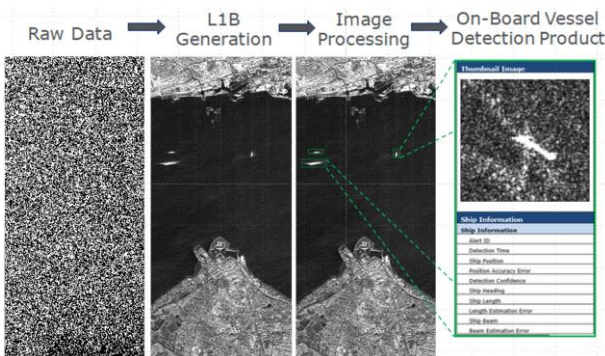


Figure 13: SAR on-board ship detection processing chain tested on TerraSAR-X EO payload data for the provision of **ship detection**

For the ship scenario, the SAR processing uses the SAR TerraSAR-X satellite data. The testing is performed in a single-board scheme. Each board processes about 400 km$^2$ at ~4m resolution. The entire on-board processing chain (see Figure 13) takes less than 40 s running on a single Xilinx Zynq US+ board. Including the communication of alerts (ship detection

and thumbnail image) through a global communications link, the total time is for alert generation and delivery is typically less than 1.5 minutes, and below 1 minute in the case that the number of alerts to be transmitted is small (i.e., less than 20 ship alerts). More information on the SAR processing chain can be found in [32].

*Extreme Weather Scenario Results*

The ATB has also been used in ground testing to quantify the latency of the extreme weather service.

For the extreme weather scenario for wind speed and wave height, using the satellite TerraSAR-X data, the latency for the product provision is similar to that for the ship scenario with SAR. The total time for alert generation and delivery is less than 1.5 minutes. More information can be found in [32].

For the extreme weather nowcasting for convective storm detection and monitoring, using SEVIRI optical VIS/TIR data, the total time for alert generation (see Figure 11) and delivery is less than 1 minute, noting that in this case, due to the GEO satellite use, both a direct-to-ground and global communications link suffice. More information on the extreme weather processing chain and scenario in can be found in [32].
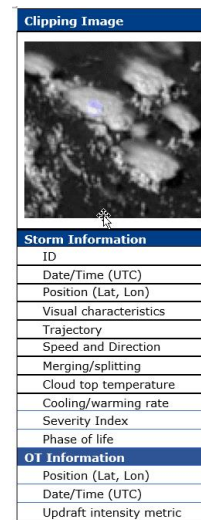


**Figure 11:Optical on-board Extreme Weather Nowcasting tested on MSG SEVIRI payload data for the provision of extreme weather alerts similar to that of the EUMETSAT RDT product: example storm thumbnail and support data.**

## 5.  Conclusions

In this paper, we have presented the results of the experimental evaluation of the innovative elements of EO-ALERT's data processing chain. The verification results show that the demanding objective of providing EO products with latencies below 5 min can be achieved. Furthermore, the results show **global EO product latencies below 1 min in realistic scenarios**.

The architecture, although demonstrated for the generation of alerts in two example scenarios, ship detection and extreme weather monitoring, remains quite general and can be easily adapted to alternative scenarios.

The proposed architecture can be efficiently implemented relying on a hybrid solution combining space qualified components and high-performance COTS components and using available communication links. The on-board architecture and technologies reach Technology Readiness Level (TRL) 4 maturity for HW components, and TLR 5 for all SW implementations.

The paper also discusses the implementation on an Avionic Test Bench (ATB) for the validation of the integrated technologies chain. The overall results of the entire project, including the experimental validation of the avionics test bench, will be presented to end-users and possible commercial partners at the upcoming final EO-ALERT workshop.

## References

[1] Kerr M., Cornara S., Latorre A., Tonetti S., Fiengo A., Gomez de Aguero S., Bravo J. I., Velotto D., Breit H., Balss U., Koudelka O., Teschl F., Magli E., Bianchi T., Freddi R., Benetti M., Fabrizi R., Fraile S., Marcos C., "EO-ALERT: A Novel Flight Segment Architecture for EO Satellites Providing Very Low Latency Data Products", ESA Phi-week 2019, 9-13 September, ESA-ESRIN, Frascati, Rome

[2] Autonès, F., Moisselin, J.-M., (2019), Algorithm Theoretical Basis Document for the Convection Product Processors of the NWC/GEO (https://www.nwcsaf.org/web/guest/scientificdocumentation)

[3] M. Kerr, S. Tonetti, S. Cornara, J. I. Bravo, R. Hinz, A. Latorre, F. Membibre, C. Solimini, S. Wiehle, H. Breit, B. Tings, O. Koudelka, F. Teschl, E. Magli, T. Bianchi, A. Migliorati, P. Motto Ros, M. Caon, R. Freddi, M. Benetti, F. Milani, G. Curci, S. Fraile, L. Garcia, C. Marcos, A. Fiengo, "EO-ALERT: A Novel Architecture for the Next Generation of Earth Observation Satellites Supporting Rapid Civil Alerts", IAC-20-D1.2.5, 71st International Astronautical Congress, The CyberSpace Edition, 12-14 October 2020.

[4] S. Tonetti, S. Cornara, M. Kerr, G. Vicario de Miguel, S. Fraile, M. Díez, H. Breit, S. Wiehle, C. Marcos Martín, C. Solimini, "Novel Operational Scenarios for the Next-Generation Earth Observation Satellites Supporting On-Board Processing for Rapid Civil Alerts", IAC-21-B6.2.9, 72nd International Astronautical Congress (IAC), Dubai, United Arab Emirates, 25-29 October 2021.

## Acknowledgements

[5] Saltikoff, E., Haase, G., Delobbe, L., Gaussiat, N., Martet, M., Idziorek, D., Stephan, K. (2019). OPERA the Radar Project. *Atmosphere*, *10*(6), 320. https://doi.org/10.3390/atmos10060320

[6] Steiner et al. (1995). Climatological characterization of three-dimensional storm structure from operational radar and rain gauge data. Journal of Applied Meteorology, 34(9), 1978-2007.

[7] R. Hinz, Á. Morón, J. I. Bravo, M. Kerr, C. Marcos, A. Latorre, F Membibre (2021). *Towards Very-Low Latency Storm Nowcasting through AI-Based On-Board Satellite Data Processing*, 1st workshop on Complex Data Challenges in Earth Observation (CDCEO) 2021.

[8] Kristopher M. Bedka, (2011). Overshooting cloud top detections using MSG SEVIRI Infrared brightness temperatures and their relationship to severe weather over Europe. Atmospheric Research 99, 175–189.

[9] Setvák, M., Radová, M., Kaňák, J., Valachová, M., Bedka, K. M., Šťástka, J., Kyznarová, H. (2014). Comparison of the MSG 2.5-minute Rapid Scan Data and Products derived from these, with Radar and Lightning Observations. EUMETSAT Proceedings, (September), 22–26.

[10] M. Kerr, S. Tonetti, S. Cornara, J I Bravo, R. Hinz, A. Latorre, F. Membibre, A. Ramos, A. Moron, C. Solimini, "A Novel Satellite Architecture for the Next Generation of Earth Observation Satellites Supporting Rapid Alerts", SSC21-VIII-07, 35th Annual Small Satellite Conference, 7-12 Aug., 2021.

[11]     A. Latorre, F. Membibre, J.I. Bravo, R. Hinz, A. Ramos, M. Kerr, "On-board Low Latency Processing of Earth Observation Products in a Multi-board Scheme Using Multi-core and FPGA-based Architecture", IAC-20-D1.3.7, 71st International Astronautical Congress, The CyberSpace Edition, 12-14 October 2020.

[12]     R. Hinz, J.I. Bravo, M. Kerr, C. Marcos, A. Latorre, F. Membibre, "EO-ALERT: Machine Learning-Based On-Board Satellite Processing for Very-Low Latency Convective Storm Nowcasting", ECMWF-ESA Workshop on Machine Learning for Earth System Observation and Prediction, 2020.

[13]     Otsu, N. (1979). A threshold selection method from gray-level histograms. IEEE transactions on systems, man, and cybernetics, 9(1), 62-66

[14]     Wu, K. & al. (2009). Optimizing two-pass connected-component labeling algorithms. Pattern Analysis and Applications, 12(2), 117-135

[15]     Kim et al., (2017) Detection of Tropical Overshooting Tops Using Himawari-8 Imagery. Remote Sens 9(7), 685, 2017.

[16]     Raney, R.K. & al. (1994) "Precision SAR Processing Using Chirp Scaling," IEEE Transactions on Geoscience and Remote Sensing (TGRS), Vol. 32, pp. 786-799

[17]     Bamler, R (1992) A Comparison of Range-Doppler and Wavenumber Domain SAR Focusing Algorithms, IEEE Trans. On Geoscience and Remote Sensing, 30 (4), 706-713

[18]     Tings, B. & al. (2016) Dynamically adapted ship parameter estimation using TerraSAR-X images, Int J Remote Sens, 37:9, 1990-2015, DOI: 10.1080/01431161.2015.1071898

[19]     Li, X.-M., Lehner, S. (2014) Algorithm for sea sur-face wind retrieval from TerraSAR-X and TanDEM-X data, IEEE Trans Geosci Remote Sens., 52, 5, 2930-2941

[20]     Pleskachevsky, A.L. & al. (2016) Meteo-Marine Parameters for Highly Variable Environment in Coastal Regions from Satellite Radar Images. ISPRS J. Photogr. Remote Sens., 119, 464–484

[21]     Consultative Committee for Space Data Systems (CCSDS), "Low-Complexity Lossless and Near- Lossless Multispectral and Hyperspectral Image Compression," Blue Book, no. 1, February 2019

[22]     A. Migliorati & al., "Selective encryption in the CCSDS standard for lossless and near-lossless multispectral and hyperspectral image compression",

Proceedings Volume 11533, Image and Signal Processing for Remote Sensing XXVI; 1153312 (2020)

[23]     M. Caon, P. Motto Ros, T. Bianchi, M. Martina and E. Magli, "Low latency on-board data handling for earth observation satellites using off-the-shelf components," in 2nd European Workshop on On-Board Data Processing, 2021.

[24]     P. Motto Ros, M. Caon, T. Bianchi, M. Martina and E. Magli, "High-level synthesis of a single/multi-band optical and SAR image compression and encryption hardware accelerator," in International Geoscience and Remote Sensing Symposium, Brussels, 2021.

[25]     M. Caon, P. Motto Ros, M. Martina, T. Bianchi, E. Magli, F. Membibre, A. Ramos, A. Latorre, M. Kerr, S. Wiehle, H. Breit, D. Günzel, S. Mandapati, U. Balss and B. Tings, "Very low latency architecture for earth observation satellite onboard data handling, compression, and encryption," in International Geoscience and Remote Sensing Symposium, Brussels, 2021.

[26]     https://www.addvaluetech.com/inter-satellite-data-relay-system-idrs/

[27]     Autonès, F., Claudon, J.-M. (2019). Validation report of the Convection Product Processors of the NWC/GEO. (https://www.nwcsaf.org/web/guest/scientificdocumentation)

[28]     Autonès, F. (2016). Validation report of the Convection Product Processors of the NWC/GEO. (https://www.nwcsaf.org/web/guest/scientificdocumentation)

[29]     Nikolai Dotzek, Pieter Groenemeijer, Bernold Feuerstein, Alois M. Holzer (2009). Overview of ESSL's severe convective storms research using the European Severe Weather Database ESWD. Atmospheric Research 93, 575–586.

[30]     F. Membibre, et. al., "PIL testing of the Optical On-board Image Processing Solution for EO-ALERT", ESA OBDP, 2021.

[31]     A. Latorre, et. al., "On-board Low Latency Processing of Earth Observation Products in a Multi-board Scheme Using Multi-core and FPGA-based Architecture", IAC 2020, October 2020.

[32]     S. Wiehle, et. Al., "SAR satellite on-board ship, wind, and sea state detection", IGARSS, 2021.